Research article

Chenglong Zheng, Jie Li, Guocui Wang, Jingyu Liu, Jitao Li, Zhen Yue, Hongliang Zhao, Xuanruo Hao, Yating Zhang*, Yan Zhang* and Jianquan Yao*

All-dielectric metasurfaces capable of dual-channel complex amplitude modulation

https://doi.org/10.1515/nanoph-2021-0349
Received July 6, 2021; accepted July 26, 2021;
published online August 11, 2021

Abstract: One compound metasurface with multiple functions and precise complex amplitude modulation is beneficial to photonic integration. Here, all-silicon bifunctional metasurfaces capable of independent amplitude and phase modulation in two circular polarized channels are proposed, which encode complex amplitude information by integrating propagation phase and Pancharatnam-Berry phase. A switchable power-controllable axial bifocal metalens directly illustrates the feasibility of the proposed modulation scheme. Another switchable power-controllable horizontal/vertical bifocal metalens characterizes the versatility and flexibility of this approach. The experimental results agree well with the simulations and theoretical expectations. In addition, we also discuss the broadband performance of the proposed metalens and the dynamic focusing behavior under optical pumping. The proposed approach can directly generate editable amplitude and phase profiles and can find applications in dynamic holography, dynamic display, and other fields.

Keywords: all-dielectric metasurface; complex amplitude modulation; decoupling; terahertz.

***Corresponding authors: Yating Zhang and Jianquan Yao**, Key Laboratory of Opto-Electronics Information Technology (Tianjin University), Ministry of Education, School of Precision Instruments and Opto-Electronics Engineering, Tianjin University, No. 92 WeiJin Road, Tianjin, 300072, China; and **Yan Zhang**, Department of Physics, Beijing Key Laboratory for Metamaterials and Devices, Key Laboratory of Terahertz Optoelectronics, Ministry of Education, and Beijing Advanced Innovation Center for Imaging Technology, Capital Normal University, Beijing, 100048, China, E-mail: yating@tju.edu.cn (Y. Zhang), jqyao@tju.edu.cn (J. Yao), yzhang@mail.cnu.edu.cn (Y. Zhang)

Chenglong Zheng, Jie Li, Jitao Li, Zhen Yue, Hongliang Zhao and Xuanruo Hao, Key Laboratory of Opto-Electronics Information Technology (Tianjin University), Ministry of Education, School of Precision Instruments and Opto-Electronics Engineering, Tianjin University, No. 92 WeiJin Road, Tianjin, 300072, China. https://orcid.org/0000-0001-5754-5448 (C. Zheng). https://orcid.org/0000-0002-5849-9903 (J. Li)

Guocui Wang, Beijing Engineering Research Center for Mixed Reality and Advanced Display, School of Optics and Photonics, Beijing Institute of Technology, Beijing, 100081, China; and Department of Physics, Beijing Key Laboratory for Metamaterials and Devices, Key Laboratory of Terahertz Optoelectronics, Ministry of Education, and Beijing Advanced Innovation Center for Imaging Technology, Capital Normal University, Beijing, 100048, China

Jingyu Liu, Department of Physics, Beijing Key Laboratory for Metamaterials and Devices, Key Laboratory of Terahertz Optoelectronics, Ministry of Education, and Beijing Advanced Innovation Center for Imaging Technology, Capital Normal University, Beijing, 100048, China

1 Introduction

Metasurfaces, the two-dimensional form of metamaterials, are planar optical elements composed of artificially designed meta-atoms. Because of the powerful manipulation of electromagnetic waves, they have attracted extensive attentions of researchers [1–3]. Unlike traditional optical elements that require a long propagation distance to accumulate phase shift, metasurfaces can introduce an abrupt phase discontinuity at the interface to achieve phase modulation [1]. The ways of manipulating scattered light can be divided into resonance phase, Pancharatnam-Berry (PB) phase, propagation phase, and detour phase [4–8]. These planar microstructure arrays with subwavelength scale have the capability of full 2π phase modulation, and has shown strong application potential in many interesting devices, such as flat metalens [9, 10], holography [11–13], vortex generators [14–18] image differentiators [19–21], wave plates [22, 23].

In addition to being a device that produces a certain specific function, recently, researchers have proposed many multiplexed and multifunctional metasurfaces, which integrate degrees of freedom such as polarization, wavelength, incident angle, and time series [24–28]. Metasurfaces with anisotropic response provide an effective way for the integration of different optical functions. Rotating anisotropic meta-atoms can introduce additional geometric phase for circular polarizations. However, the left-handed circularly

polarized (LCP) and right-handed circularly polarized (RCP) incidences are mutually locked [29]. The proposal of so-called spin-decoupling, which combines PB phase and propagation phase, overcomes this limitation [25, 30–35]. Completely independent functions can be realized in two circular polarized channels, such as polarization-switching holograms [25], switchable vortices with different topological charges [30], independent switching between two arbitrary visible accelerating light beams [31], and so on. In addition, multiple channels or functions can also be integrated through segmented, interleaved, and multi-layer designs [36, 37].

To completely control the propagation of electromagnetic wave, in addition to the parameters of polarization and phase, amplitude is essential. Compared with those phase-only metasurfaces, devices that can simultaneously modulate amplitude and phase distributions have better performance of wavefront shaping, and have advantages in high-quality holography, generation of complex light fields, and so on [18, 38–41]. *C*-shaped meta-atoms were proposed to achieve amplitude and phase modulation in terahertz (THz) band [38]. A complex amplitude modulation metasurface working at dual wavelengths was reported in Ref. [41]. *X*-shaped meta-atoms were used to achieve such modulation [39]. Chiral-assisted metasurfaces were proposed for independent phase, amplitude and polarization control [40]. Most of these metasurfaces are reflective or multilayer designs, and they are designed for a specific polarization.

In this article, we propose all-silicon bifunctional metasurfaces that can achieve independent amplitude and phase modulation in two circularly polarized channels. These metasurfaces combine propagation phase and PB phase, and encode complex amplitude information into these two channels. As functional demonstrations, we design two metasurfaces: (1) a switchable power-controllable axial bifocal metalens; (2) a switchable power-controllable horizontal/vertical bifocal metalens. The experimental results are in good agreement with the simulations. The broadband performance of the proposed metalens and the dynamic focusing behavior under optical pumping conditions are also studied. Such a scheme provides a new choice for the development of multifunctional photonic devices.

2 Results and discussions

Figure 1 shows the schematic of the proposed bifunctional metasurface with complete amplitude and phase modulation. Here, we take the switch of two foci with controllable amplitude ratio as an example to show the independent complex amplitude modulations in two circular polarizations. The polarization-dependent bifunctional design relies on the principle of spin-decoupling, which combines the degree of freedom of PB phase on the basis of propagation phase. Until now, there have been several reports about the complex amplitude modulation on a phase-only spatial light modulator (SLM) [42, 43], which enables simultaneous amplitude and phase modulation by multiplying the desired amplitude distribution with a blazed grating. Let us assume that the required complex amplitude is expressed as:

$$U(x,y) = A(x,y)\exp\left[i\varphi(x,y)\right] \tag{1}$$

Where $A(x, y)$ and $\varphi(x, y)$ are amplitude and phase information, respectively. In order to completely manipulate the target field, we use a technique introduced in Ref. [42] and encode the required amplitude and phase information onto a metasurface. Therefore, the coded complex amplitude of the proposed metasurface can be expressed as:

$$T(x,y) = \exp\left[i\phi(x,y)\right] = \exp\left[iA(x,y)\varphi(x,y)\right] \tag{2}$$

Here, $T(x, y)$ represents the total transmission function, and $\phi(x, y)$ is the encoding phase combining the amplitude information $A(x, y)$ and the original phase information $\varphi(x, y)$.

The basic meta-atom of the all-silicon metasurface is illustrated in Figure 2(a), which is a rectangular pillar with permittivity of $\varepsilon = 11.9$ and a height of $h = 200$ μm. The phase responses can cover a 2π range under the x and y polarized illuminations by changing the length L_1 and width L_2, respectively. The simulated transmission amplitudes and phase shifts of the selected fifteen meta-atoms at 0.9 THz are shown in Figure 2(b), which are simulated using CST Microwave Studio. The transmission phase shifts are in increment of $\pi/8$ and the phase difference between x and y polarization is π. And all of the transmission amplitudes remain around 0.7 with a small fluctuation. Figure 2(c) shows the simulated side view (xoz) of the phase distributions in four silicon pillars (corresponding to the #1, #5, #9, and #13 in Figure 2(b)) under the x and y polarized illuminations, respectively, at 0.9 THz. It can be seen that, from #1 to #13, the phase shifts gradually increase with the change of structural parameters under the x and y polarized illuminations. Specially, the phase differences between #1 and #9, #5 and #13 are π.

In addition to the propagation phase obtained by changing the parameters of meta-atoms, the geometric phase is introduced to realize the independently controllable circular polarization phase, which is achieved by rotating the meta-atom at a specific angle. The propagation phase and rotation angle of the meta-atom need to meet are [25]:

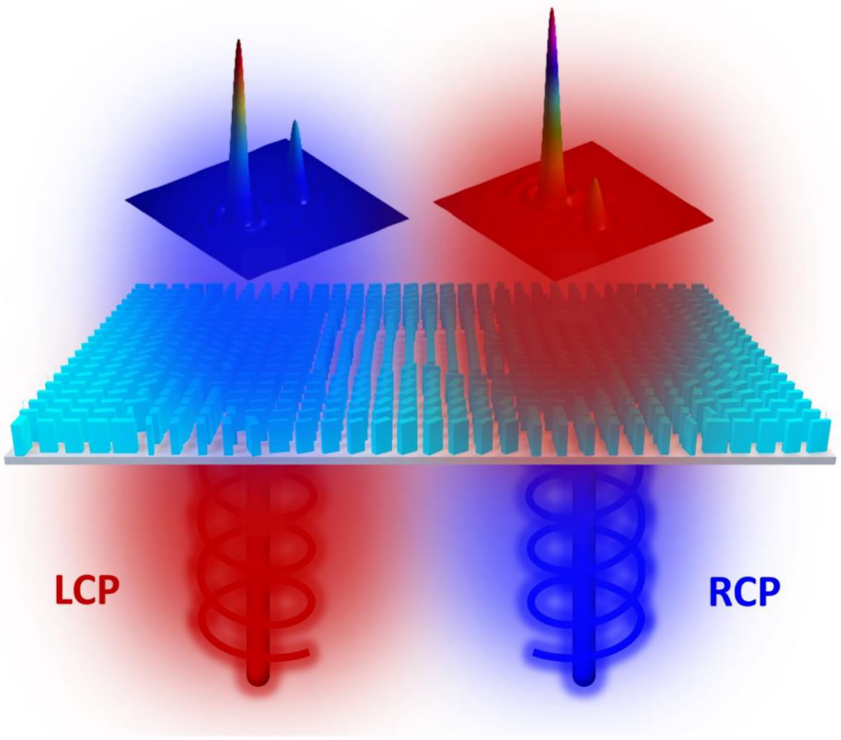

Figure 1: The schematic of a bifunctional metasurface with complete amplitude and phase modulation.
For the LCP incidence, the transmitted RCP field contains two foci with an amplitude ratio of 3:2 along *x* axis. For the RCP incidence, the transmitted LCP field contains two foci with an amplitude ratio of 2:1 along *y* axis.

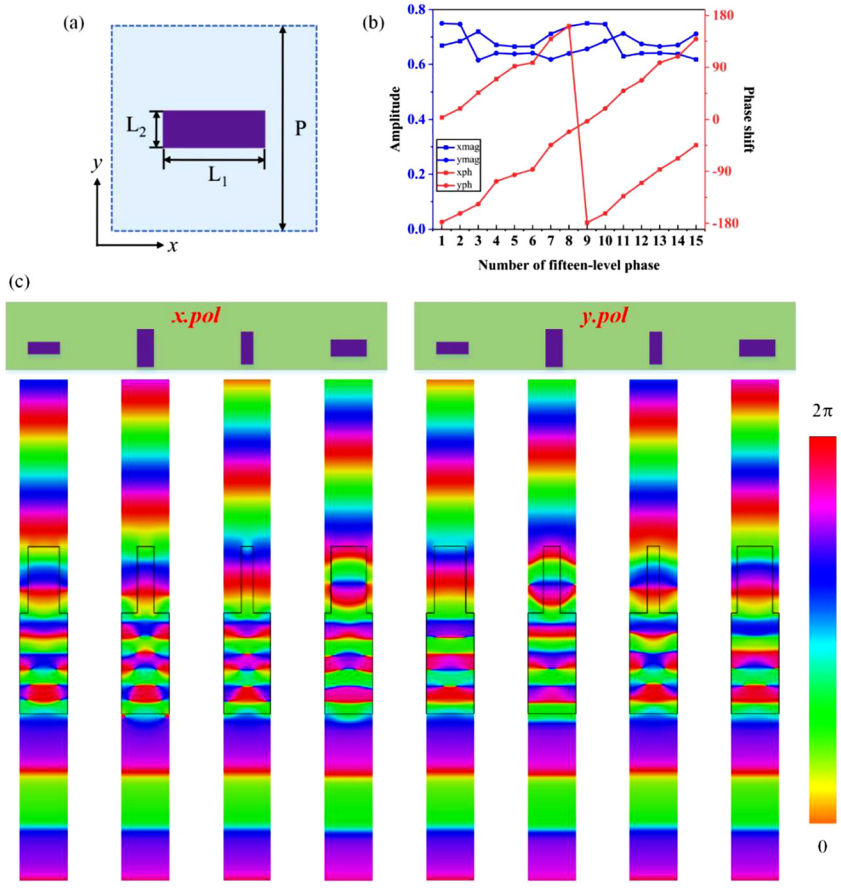

Figure 2: Characterization of the designed meta-atoms.
(a) Schematic of the rectangular-shape silicon pillar. (b) Simulated transmission amplitudes and phase shifts of the selected fifteen meta-atoms at 0.9 THz. (c) Simulated side view (*xoz*) of the phase distributions in four silicon pillars (#1: L_1 = 98 μm, L_2 = 38 μm; #5: L_1 = 52 μm, L_2 = 116 μm; #9: L_1 = 38 μm, L_2 = 100 μm; #13: L_1 = 110 μm, L_2 = 52 μm) under the *x* and *y* polarized illumination, respectively, at 0.9 THz.

$$\begin{cases} \varphi_x = (\varphi_{\mathrm{LCP}} + \varphi_{\mathrm{RCP}})/2 \\ \varphi_y = (\varphi_{\mathrm{LCP}} + \varphi_{\mathrm{RCP}})/2 - \pi \\ \theta = (\varphi_{\mathrm{LCP}} + \varphi_{\mathrm{RCP}})/4 \end{cases} \tag{3}$$

Where φ_x (φ_y) represents the phase response under x (y) polarized incidence, φ_{LCP} (φ_{RCP}) represents the required circularly polarized phase profile, and θ is the rotation angle of the meta-atom.

By using these rectangular-shape silicon pillars as the basic building blocks, the proposed bifunctional metasurfaces can realize switchable amplitude-phase modulation. Next, we will use the generation of power-controllable axial and horizontal/vertical bi-foci as examples to characterize the feasibility and flexibility of this approach. In addition to generating such switchable power-controllable

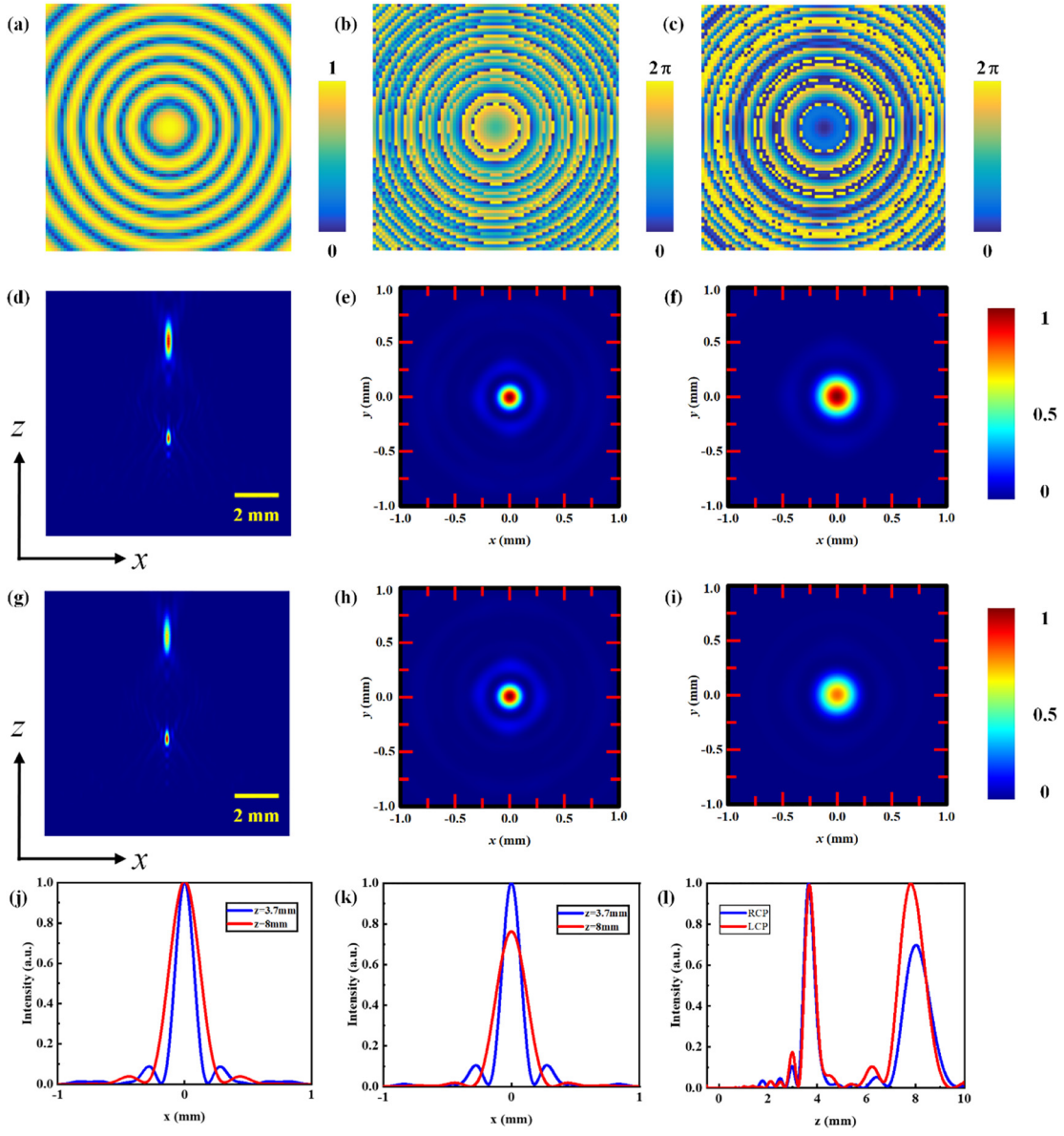

Figure 3: Design and characterization of the axial bifocal metalens.
(a) The required amplitude distribution of the target field. (b) The required phase distribution of the target field. (c) The coded phase distribution. (d–f) The transmitted field profiles under the LCP illumination: (d) The axial intensity profile. (e) The simulated intensity profile of the first focal plane f_1. (f) The simulated intensity profile of the second focal plane f_2. (g–i) The transmitted field profiles under the RCP illumination: (g) The axial intensity profile. (h) The simulated intensity profile of the first focal plane f_1. (i) The simulated intensity profile of the second focal plane f_2. (j) The intensity profiles across the two focal planes under the LCP illumination. (k) The intensity profiles across the two focal planes under the RCP illumination. (l) The comparison of intensity profiles along the optical axis under the LCP/RCP illumination.

bifocal or multifocal metalens, such approach can also be used to generate complex light fields, high-quality holography, and other applications that require complete manipulation of the light field.

3 Proof of concept demonstrations

3.1 Switchable power-controllable axial bifocal metalens

First, a switchable intensity-ratio axial bifocal metalens has been designed employing the proposed method. For the LCP incidence, the proposed metalens is encoded with the required amplitude and phase information of the target field. While for the RCP illumination, only the phase information is encoded. Through such a comparison, not only the bifunctional characteristic of this approach can be shown, but also the feasibility of its complex amplitude modulation can be characterized.

The required complex amplitude distributions can be described as:

$$\begin{aligned}
\varphi_1 &= \frac{2\pi}{\lambda}\left(\sqrt{r^2+f_1^2}-f_1\right)\\
\varphi_2 &= \frac{2\pi}{\lambda}\left(\sqrt{r^2+f_2^2}-f_2\right)\\
E &= \alpha_1\exp\left(i\varphi_1\right)+\alpha_2\exp\left(i\varphi_2\right)\\
A &= abs\left(E\right)\\
\varphi_{RL} &= angle\left(E\right)\\
\varphi_{LR} &= abs\left(E\right)\times angle\left(E\right)
\end{aligned} \tag{4}$$

Where φ_1 (φ_2) represents the phase distribution for generating a focused beam with a focal length of f_1 (f_2), λ is the designed wavelength corresponding to 0.9 THz, the focal length is set to f_1 = 3.7 mm, f_2 = 8 mm, and α_1 and α_2 are amplitudes of the two foci (α_1:α_2 = 1:1). E represents the designed complex amplitude distribution, A represents the amplitude information of the target field, φ_{RL} (φ_{LR}) represents the phase distribution of the transmitted LCP (RCP) component in response to RCP (LCP) incidence. Figure 3(a)–(c) show the required amplitude (A), phase (φ_{RL}), and coded phase (φ_{LR}) distributions, respectively.

Let's first consider the case of the LCP incidence. The simulated axial intensity profile is shown in Figure 3(d). As the theoretical design, there are two foci are generated along the optical axis. Figure 3(e) and (f) show the simulated intensity profiles at $z = f_1$ and $z = f_2$, respectively. The intensity profiles across these two focal planes are plotted in Figure 3(j). It can be seen that these two foci have the same peak intensities. And full width at half maxima (FWHM) of the first focus is less than that of the second focus. Next, we will discuss the case of the RCP incidence. As a contrast, we only encode the phase information of the target light field in this channel. The corresponding intensity profiles are shown in Figure 3(g)–(i). The intensity profiles across the two focal planes are plotted in Figure 3(k). It is observed that, although two foci are generated at the set locations, their peak intensities are not the same. The comparison of intensity profiles along the optical axis under the LCP/RCP illumination are plotted in Figure 3(l). It is obvious that the channel encoding both intensity and phase information generates two foci with equal intensity, while the other channel can generate only two foci and cannot modulate the intensity profile of the target. This comparison can directly illustrate the feasibility of this complex amplitude modulation scheme. However, it should be noted that encoding amplitude information will cause some energy loss, resulting in a slight decrease in focusing efficiency.

3.2 Switchable power-controllable horizontal/vertical bifocal metalens

To validate the versatility and flexibility of this approach, a second metalens is designed to generate polarization-dependent power-controllable multiple foci. For this metalens, two independent functions are designed in the two circularly polarized channels: two foci with amplitude ratio of α_1:α_2 = 3:2 (power allocation I_1:I_2 = 2.25:1) along the x axis are generated under the LCP incidence, and two foci with amplitude ratio of α_3:α_4 = 2:1 (power allocation I_3:I_4 = 4:1) along the y axis are generated under the RCP incidence. To realize such bifunctional device, the required coded complex amplitude distributions are described as:

$$\begin{aligned}
\varphi_1 &= \frac{2\pi}{\lambda}\left(\sqrt{(x+\xi)^2+y^2+f^2}-f\right)\\
\varphi_2 &= \frac{2\pi}{\lambda}\left(\sqrt{(x-\xi)^2+y^2+f^2}-f\right)\\
\varphi_3 &= \frac{2\pi}{\lambda}\left(\sqrt{x^2+(y+\xi)^2+f^2}-f\right)\\
\varphi_4 &= \frac{2\pi}{\lambda}\left(\sqrt{x^2+(y-\xi)^2+f^2}-f\right)\\
E_1 &= \alpha_1\exp\left(i\varphi_1\right)+\alpha_2\exp\left(i\varphi_2\right)\\
E_2 &= \alpha_3\exp\left(i\varphi_3\right)+\alpha_4\exp\left(i\varphi_4\right)\\
\varphi_{LR} &= abs\left(E_1\right)\times angle\left(E_1\right)\\
\varphi_{RL} &= abs\left(E_2\right)\times angle\left(E_2\right)
\end{aligned} \tag{5}$$

Where the factor ξ = 800 μm is introduced to generate off-axis foci, the focal length is set to f = 8 mm, and φ_{LR} (φ_{RL}) represents the phase distribution of the transmitted RCP (LCP) component in response to LCP (RCP) incidence.

The simulated axial intensity profile (*xoz*) of the transmitted RCP component under the LCP illumination is shown in Figure 4(a). It can be seen that there are two foci are generated. The simulated intensity profile at the focal plane is shown in Figure 4(e) and the intensity profile along

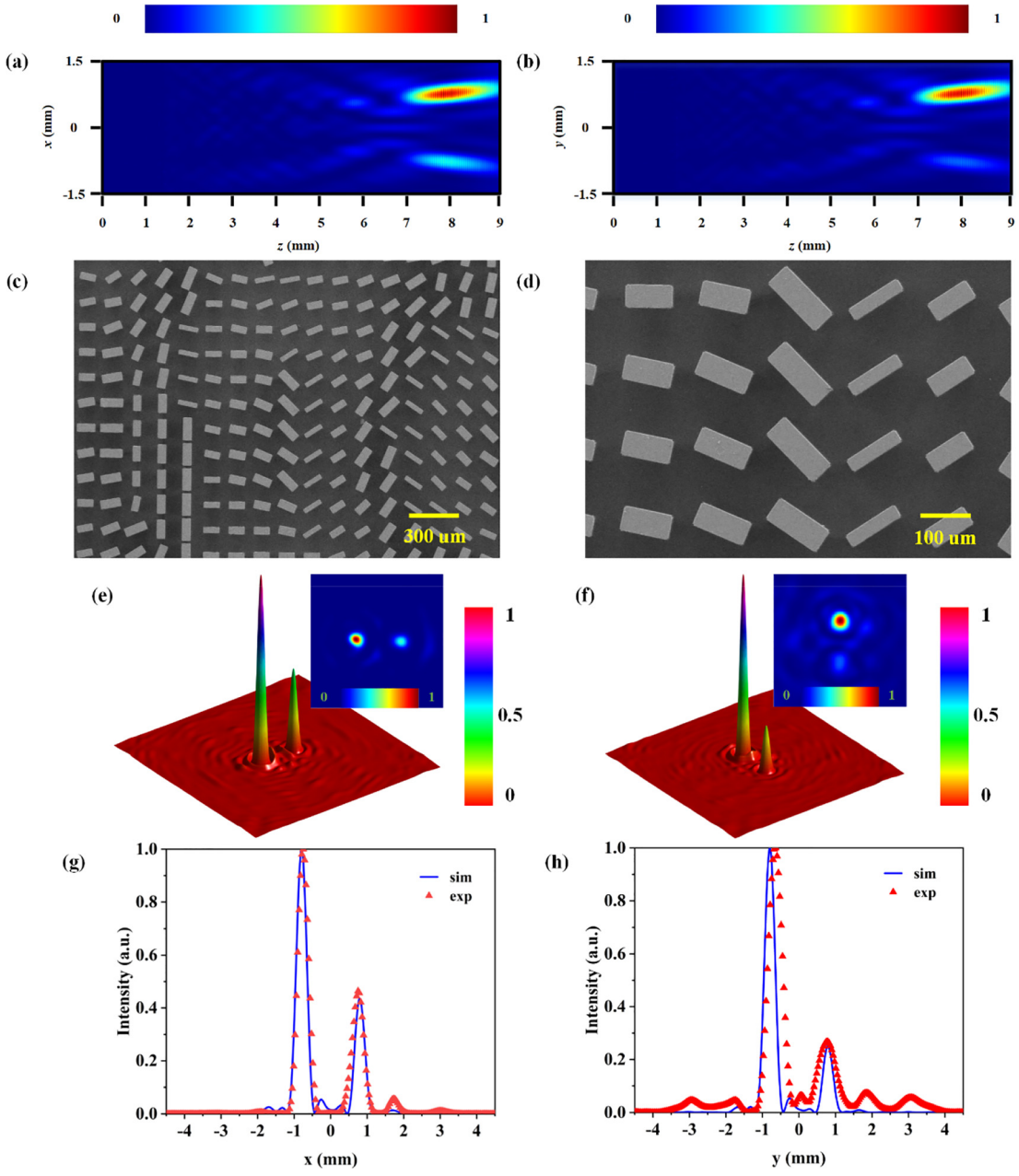

Figure 4: Characterization of the horizontal/vertical bifocal metalens.
(a) The axial intensity profile (*xoz*) of the transmitted RCP component under the LCP illumination. (b) The axial intensity profile (*yoz*) of the transmitted LCP component under the RCP illumination. (c, d) SEM images of the fabricated sample. (e) The simulated RCP intensity profile at the focal plane under the LCP illumination. The inset is the measured intensity profile. (f) The LCP intensity profile under the RCP illumination. The inset is the measured intensity profile. (g) The simulated and measured intensity profile along the *x* axis at the focal plane under the LCP illumination. (h) The simulated and measured intensity profile along the *y* axis at the focal plane under the RCP illumination.

the x axis is plotted in Figure 4(g). It's clear that the intensity ratio of the two foci is approximately 2.25:1. For the RCP incidence, there are two foci along the y axis are generated (Figure 4(b)). The corresponding simulated intensity profiles at the focal plane are shown in Figure 4(f) and (h). And the intensity ratio of the two foci is approximately 4:1. These simulated results are in good agreement with the theoretical design. In order to better verify the feasibility of our proposed design, we fabricate a sample (Figure 4(c) and (d)) and explore the optical modulation characteristics using the THz digital holographic imaging system [44]. The sample is fabricated by standard ultraviolet lithography and inductively coupled plasma (ICP) etching technology [35]. The two-dimensional THz field profiles were extracted by using balanced electro-optic detection technique and dynamic subtraction technique [45]. The amplitude and phase information can be obtained by performing Fourier transformations on the temporal signals. The measured intensity profiles under the LCP/RCP incidences are shown in the insets of Figure 4(e) and (f). And the measured intensity profiles along the x/y axis at the focal plane are plotted in Figure 4(g) and (h). It can be seen that the measured intensity profiles and the measured intensity ratios agree well with the simulations.

4 Broadband property of the proposed metalens

The broadband performance of the proposed metalens has been investigated, as shown in Figure 5. Here, the broadband performances of both circularly polarized channels are discussed. Figure 5(a) shows the axial intensity profiles (*xoz*) under the LCP illumination, where the incident frequencies are from 0.7 to 1.1 THz. When the incident

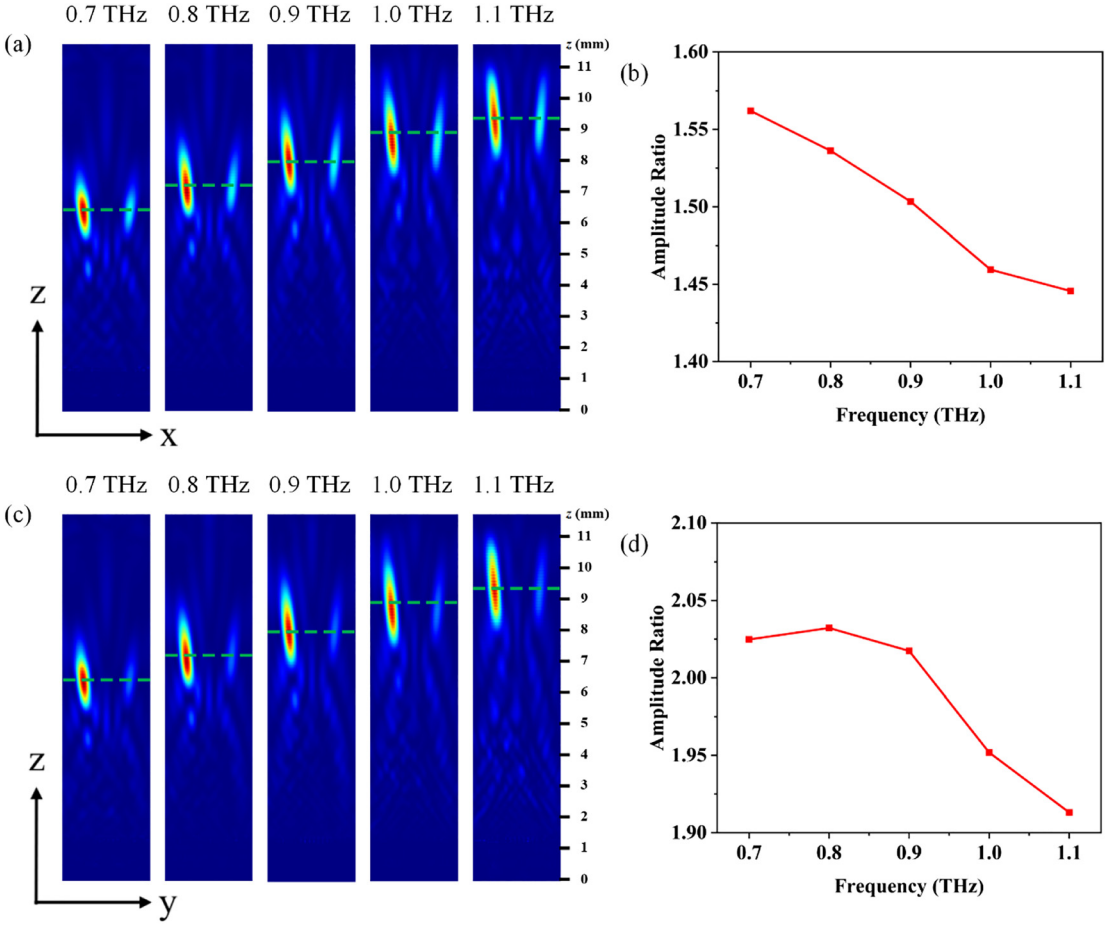

Figure 5: Characterization of broadband property of metalens.
(a) The axial intensity profiles (*xoz*) under the LCP illumination with different frequencies. (b) The amplitude ratios of the generated two foci along the x axis under the different incident frequencies. (c) The axial intensity profiles (*yoz*) under the RCP illumination with different frequencies. (d) The amplitude ratios of the generated two foci along the y axis under the different incident frequencies.

frequency is 0.9 THz, the generated two foci are at the set focal length z = 8 mm. It can be seen that the focal length increases as the incident frequency increases. Then the amplitude ratios of the generated two foci along the x axis under the different incident frequencies are plotted in Figure 5(b). Obviously, although the focal length changes with the incident frequency, the amplitude ratio of the two foci remains almost constant (α_1:α_2 = 3:2). For the RCP incidence, the corresponding axial intensity profiles (yoz) under the RCP illumination with different frequencies are shown in Figure 5(c). The change of focal length with the incident frequency has the same trend as that of the LCP incidence. The corresponding amplitude ratios along the y axis under the different incident frequencies are plotted in Figure 5(d). They almost have the same value (α_3:α_4 = 2:1). In other words, although the proposed metalens has obvious dispersion, the switchable complex amplitude modulation of the light field is still effective in a wide bandwidth.

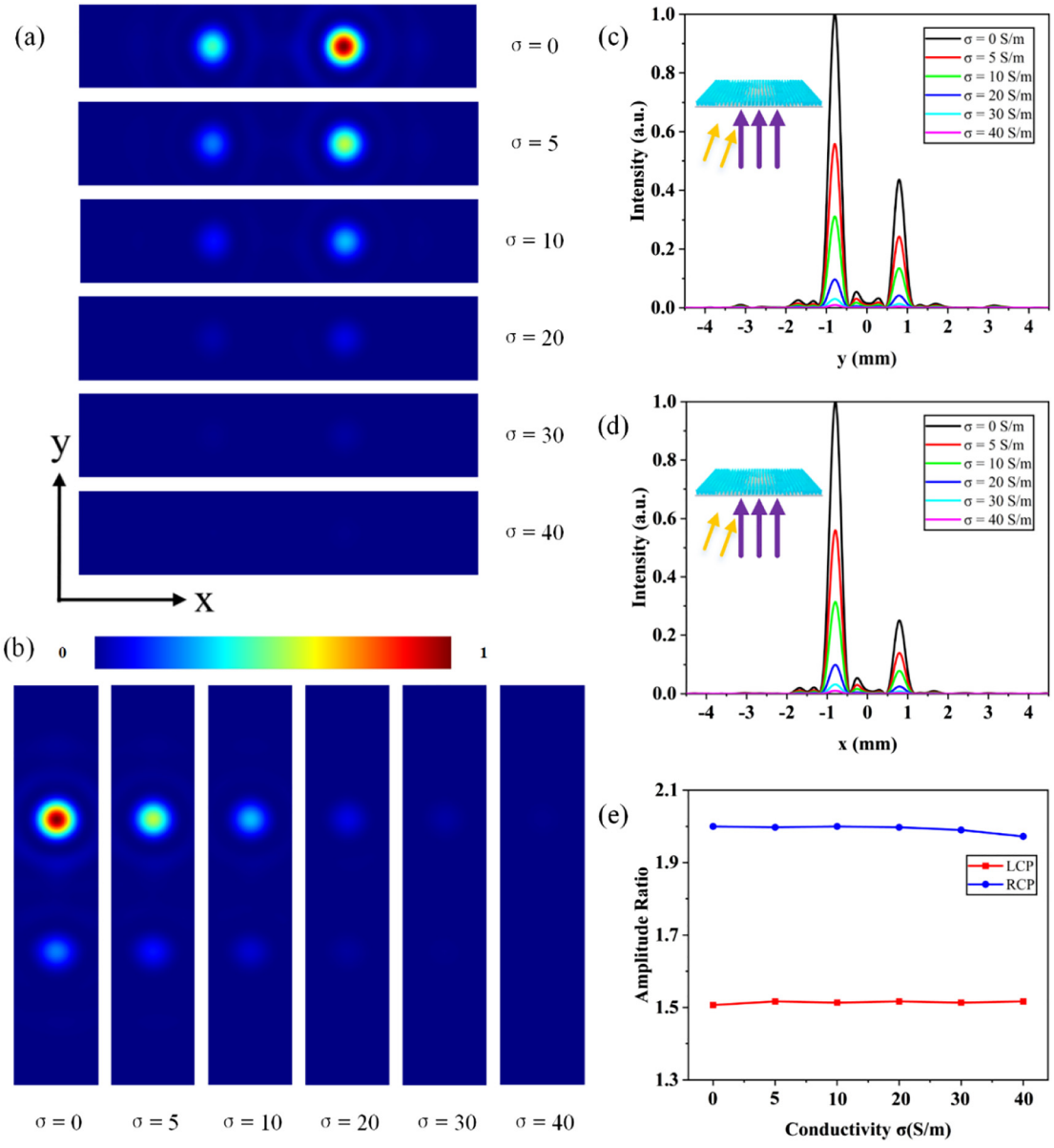

Figure 6: The dynamic behavior induced by optical pumping.
The simulated intensity profiles as the conductivity of silicon increases under the (a) LCP (b) RCP illumination. (c) The intensity profile along the x axis at the focal plane as the conductivity of silicon increases under the LCP illumination. (d) The intensity profile along the y axis at the focal plane as the conductivity of silicon increases under the RCP illumination. (e) The amplitude ratios of the generated two foci along the x/y axis as the conductivity of silicon increases.

5 Dynamic behavior of the proposed metalens induced by optical pumping

This part we will study the dynamic focusing behavior induced by optical pumping. In our previous work, dynamic chiral behaviors are characterized by optical pumping (1064 nm continuous wave) [46]. The photocarriers in the high-resistance silicon increase with the pump power increases, which will reduce the transmittance of the silicon sample. As shown in Figure 6(a), the intensity profiles as the conductivity of silicon increases under the LCP illumination are simulated. They are normalized by the peak intensity when the conductivity $\sigma = 0$ S/m. The intensity profiles along the x axis at the focal plane as the conductivity of silicon increases are plotted in Figure 6(c). It is clear that the intensities of the two foci gradually decrease to 0, as the conductivity varies from 0 S/m to 40 S/m. The corresponding intensity profiles are shown in Figure 6(b) and (d) under the RCP incidence. Similarly, the intensities of the two foci along the y axis gradually decrease as the conductivity increases. The amplitude ratios of the generated two foci along the x/y axis as the conductivity of silicon increases are plotted in Figure 6(e). Obviously, the amplitude ratios of the horizontal/vertical two foci remains almost constant, as the conductivity of silicon increases. Such dynamic behavior makes it possible for our scheme to be used in dynamic holography, dynamic maging, dynamic display, and other interesting applications.

6 Conclusion

In conclusion, we propose all-silicon bifunctional metasurfaces to achieve switchable amplitude-phase modulation in THz band, which is realized by spin-decoupling and encoding complex amplitude information. The proposed switchable power-controllable axial bifocal metalens directly illustrates the feasibility of this complex amplitude modulation scheme. The second switchable power-controllable horizontal/vertical bifocal metalens characterizes the feasibility and flexibility of this approach. In addition, the broadband performance and dynamic focusing behavior induced by optical pumping are also discussed. The proposed switchable complex amplitude modulation of the light field is effective in a wide bandwidth, and such scheme can find applications in dynamic holography, dynamic imaging, dynamic display, and other fields.

Author contributions: All the authors have accepted responsibility for the entire content of this submitted manuscript and approved submission.

Research funding: This work was supported by the National Natural Science Foundation of China (Nos. 61675147, 61735010 and 91838301), National Key Research and Development Program of China (No. 2017YFA0700202), and Basic Research Program of Shenzhen (JCYJ20170412154447469).

Conflict of interest statement: The authors declare no conflict of interest.

References

[1] N. Yu, P. Genevet, M. A. Kats, et al., "Light propagation with phase discontinuities: generalized laws of reflection and refraction," *Science*, vol. 334, no. 6054, pp. 333–337, 2011.

[2] M. Q. Mehmood, S. Mei, S. Hussain, et al., "Visible-frequency metasurface for structuring and spatially multiplexing optical vortices," *Adv. Mater.*, vol. 28, pp. 2533–2539, 2016.

[3] S. Chen, W. Liu, Z. Li, H. Cheng, and J. Tian, "Metasurface-empowered optical multiplexing and multifunction," *Adv. Mater.*, vol. 32, no. 3, p. e1805912, 2020.

[4] L. Huang, X. Chen, and H. Mühlenbernd, "Dispersionless phase discontinuities for controlling light propagation," *Nano Lett.*, vol. 12, no. 11, pp. 5750–5755, 2012.

[5] M. Khorasaninejad, A. Ambrosio, P. Kanhaiya, and F. Capasso, "Broadband and chiral binary dielectric meta-holograms," *Sci. Adv.*, vol. 2, no. 5, p. e1501258, 2016.

[6] W. Liu, Z. Li, H. Cheng, et al., "Metasurface enabled wide-angle fourier lens," *Adv. Mater.*, vol. 30, no. 23, p. 1706368, 2018.

[7] J. Lin, P. Genevet, M. A. Kats, N. Antoniou, and F. Capasso, "Nanostructured holograms for broadband manipulation of vector beams," *Nano Lett.*, vol. 13, no. 9, pp. 4269–4274, 2013.

[8] C. Min, J. Liu, T. Lei, et al., "Plasmonic nano-slits assisted polarization selective detour phase meta-hologram," *Laser Photonics Rev.*, vol. 10, no. 6, pp. 978–985, 2016.

[9] X. Chen, M. Chen, M. Q. Mehmood, et al., "Longitudinal multifoci metalens for circularly polarized light," *Adv. Opt. Mater.*, vol. 3, no. 9, pp. 1201–1206, 2015.

[10] Q. Wang, X. Zhang, Y. Xu, et al., "A broadband metasurface-based terahertz flat-lens array," *Adv. Opt. Mater.*, vol. 3, no. 6, pp. 779–785, 2015.

[11] D. Hu, X. Wang, S. Feng, et al., "Ultrathin terahertz planar elements," *Adv. Opt. Mater.*, vol. 1, pp. 186–191, 2013.

[12] G. Zheng, H. Mühlenbernd, M. Kenney, G. Li, T. Zentgraf, and S. Zhang, "Metasurface holograms reaching 80% efficiency," *Nat. Nanotechnol.*, vol. 10, pp. 308–312, 2015.

[13] B. Wang, B. Quan, J. He, et al., "Wavelength de-multiplexing metasurface hologram," *Sci. Rep.*, vol. 6, p. 35657, 2016.

[14] F. Yue, D. Wen, C. Zhang, et al., "Multichannel polarization-controllable superpositions of orbital angular momentum states," *Adv. Mater.*, vol. 29, p. 1603838, 2017.

[15] Y. Bao, J. Ni, and C. W. Qiu, "A minimalist single-layer metasurface for arbitrary and full control of vector vortex beams," *Adv. Mater.*, vol. 32, no. 6, p. 1905659, 2020.

[16] Y. Xu, H. Zhang, Q. Li, et al., "Generation of terahertz vector beams using dielectric metasurfaces via spin-decoupled phase control," *Nanophotonics*, vol. 9, no. 10, pp. 3393–3402, 2020.
[17] J. Li, G. Wang, C. Zheng, et al., "All-silicon metasurfaces for polarization multiplexed generation of terahertz photonic orbital angular momentum superposition states," *J. Mater. Chem. C*, vol. 9, pp. 5478–5485, 2021.
[18] C. Zheng, J. Li, G. Wang, et al., "Fine manipulation of terahertz waves via all-silicon metasurfaces with an independent amplitude and phase," *Nanoscale*, vol. 13, pp. 5809–5816, 2021.
[19] Q. He, F. Zhang, M. Pu, et al., "Monolithic metasurface spatial differentiator enabled by asymmetric photonic spin-orbit interactions," *Nanophotonics*, vol. 10, no. 1, pp. 741–748, 2021.
[20] Y. Zhou, H. Zheng, I. I. Kravchenko, and J. Valentine, "Flat optics for image differentiation," *Nat. Photonics*, vol. 14, no. 5, pp. 316–323, 2020.
[21] J. Zhou, H. Qian, C. F. Chen, et al., "Optical edge detection based on high-efficiency dielectric metasurface," *Proc. Natl. Acad. Sci. U.S.A.*, vol. 116, no. 23, pp. 11137–11140, 2019.
[22] C. Chen, S. Gao, X. Xiao, et al., "Highly efficient metasurface quarter-wave plate with wave front engineering," *Adv. Photonics Res.*, vol. 2, no. 3, p. 2000154, 2021.
[23] Z. Shi, A. Y. Zhu, Z. Li, et al., "Continuous angle-tunable birefringence with freeform metasurfaces for arbitrary polarization conversion," *Sci. Adv.*, vol. 6, no. 23, p. eaba3367, 2020.
[24] A. Arbabi, Y. Horie, M. Bagheri, and A. Faraon, "Dielectric metasurfaces for complete control of phase and polarization with subwavelength spatial resolution and high transmission," *Nat. Nanotechnol.*, vol. 10, pp. 937–943, 2015.
[25] J. P. Balthasar Mueller, N. A. Rubin, R. C. Devlin, B. Groever, and F. Capasso, "Metasurface polarization optics: independent phase control of arbitrary orthogonal states of polarization," *Phys. Rev. Lett.*, vol. 118, no. 11, p. 113901, 2017.
[26] C. Zhang, F. Yue, D. Wen, et al., "Multichannel metasurface for simultaneous control of holograms and twisted light beams," *ACS Photonics*, vol. 4, no. 8, pp. 1906–1912, 2017.
[27] A. Leitis, A. Tittl, M. Liu, et al., "Angle-multiplexed all-dielectric metasurfaces for broadband molecular fingerprint retrieval," *Sci. Adv.*, vol. 5, no. 5, p. eaaw2871, 2019.
[28] M. Manjappa, P. Pitchappa, N. Singh, et al., "Reconfigurable MEMS Fano metasurfaces with multiple-input–output states for logic operations at terahertz frequencies," *Nat. Commun.*, vol. 9, no. 1, p. 4056, 2018.
[29] E. Karimi, L. Marrucci, V. Grillo, and E. Santamato, "Spin-to-Orbital angular momentum conversion and spin-polarization filtering in electron beams," *Phys. Rev. Lett.*, vol. 108, no. 4, p. 044801, 2012.
[30] R. C. Devlin, A. Ambrosio, N. A. Rubin, J. P. B. Mueller, and F. Capasso, "Arbitrary spin-to-orbital angular momentum conversion of light," *Science*, vol. 358, no. 6365, pp. 896–901, 2017.
[31] Q. Fan, W. Zhu, Y. Liang, et al., "Broadband generation of photonic spin-controlled arbitrary accelerating light beams in the visible," *Nano Lett.*, vol. 19, no. 2, pp. 1158–1165, 2019.
[32] H. Xu, L. Han, Y. Li, et al., "Completely spin-decoupled dual-phase hybrid metasurfaces for arbitrary wavefront control," *ACS Photonics*, vol. 6, no. 1, pp. 211–220, 2019.
[33] Y. Xu, Q. Li, X. Zhang, et al., "Spin-Decoupled multifunctional metasurface for asymmetric polarization generation," *ACS Photonics*, vol. 6, no. 11, pp. 2933–2941, 2019.
[34] J. Li, C. Zheng, G. Wang, et al., "Circular dichroism-like response of terahertz wave caused by phase manipulation via all-silicon metasurface," *Photonics Res.*, vol. 9, no. 4, pp. 567–573, 2021.
[35] C. Zheng, J. Li, G. Wang, et al., "All-dielectric chiral coding metasurface based on spin-decoupling in terahertz band," *Nanophotonics*, vol. 10, no. 4, pp. 1347–1355, 2021.
[36] E. Maguid, I. Yulevich, D. Veksler, V. Kleiner, M. L. Brongersma, and E. Hasman, "Photonic spin-controlled multifunctional shared-aperture antenna array," *Science*, vol. 352, no. 6290, pp. 1202–1206, 2016.
[37] H. Cheng, Z. Liu, S. Chen, and J. Tian, "Emergent functionality and controllability in few-layer metasurfaces," *Adv. Mater.*, vol. 27, no. 36, pp. 5410–5421, 2015.
[38] L. Liu, X. Zhang, M. Kenney, et al., "Broadband metasurfaces with simultaneous control of phase and amplitude," *Adv. Mater.*, vol. 26, pp. 5031–5036, 2014.
[39] G. Y. Lee, G. Yoon, S. Y Lee, et al., "Complete amplitude and phase control of light using broadband holographic metasurfaces," *Nanoscale*, vol. 10, pp. 4237–4245, 2018.
[40] H. Xu, G. Hu, L. Han, et al., "Chirality-assisted high-efficiency metasurfaces with independent control of phase, amplitude, and polarization," *Adv. Opt. Mater.*, vol. 7, no. 4, p. 1801479, 2019.
[41] J. Ding, S. An, B. Zheng, and H. Zhang, "Multiwavelength metasurfaces based on single-layer dual-wavelength meta-atoms: toward complete phase and amplitude modulations at two wavelengths," *Adv. Opt. Mater.*, vol. 5, no. 10, p. 1700079, 2017.
[42] J. A. Davis, D. M. Cottrell, J. Campos, M. J. Yzuel, and I. Moreno, "Encoding amplitude information onto phase-only filters," *Appl. Opt.*, vol. 38, no. 23, pp. 5004–5013, 1999.
[43] E. Bolduc, N. Bent, E. Santamato, E. Karimi, and R. W. Boyd, "Exact solution to simultaneous intensity and phase encryption with a single phase-only hologram," *Opt. Lett.*, vol. 38, no. 18, pp. 3546–3549, 2013.
[44] X. Wang, Y. Cui, W. Sun, J. Ye, and Y. Zhang, "Terahertz polarization real-time imaging based on balanced electro-optic detection," *J. Opt. Soc. Am. A*, vol. 27, no. 11, pp. 2387–2393, 2010.
[45] Z. Jiang, X. Xu, and X. Zhang, "Improvement of terahertz imaging with a dynamic subtraction technique," *Appl. Opt.*, vol. 39, no. 17, pp. 2982–2987, 2000.
[46] C. Zheng, J. Li, S. Wang, et al., "Optically tunable all-silicon chiral metasurface in terahertz band," *Appl. Phys. Lett.*, vol. 118, no. 5, p. 051101, 2021.